

Geometric calibration of the circle-plus-arc trajectory

Stefan Hoppe¹, Frédéric Noo², Frank Dennerlein², Günter Lauritsch³
and Joachim Hornegger¹

¹ Institute of Pattern Recognition, University of Erlangen-Nuremberg, Germany

² UCAIR, Department of Radiology, University of Utah, UT, USA

³ Siemens AG, Medical Solutions, Forchheim, Germany

E-mail: hoppe@informatik.uni-erlangen.de

Received 9 August 2007, in final form 19 October 2007

Published 12 November 2007

Online at stacks.iop.org/PMB/52/6943

Abstract

In this paper, a novel geometric calibration method for C-arm cone-beam scanners is presented which allows the calibration of the circle-plus-arc trajectory. The main idea is the separation of the trajectory into two circular segments (circle segment and arc segment) which are calibrated independently. This separation makes it possible to reuse a calibration phantom which has been successfully applied in clinical environments to calibrate numerous routinely used C-arm systems. For each trajectory segment, the phantom is placed in an optimal position. The two calibration results are then combined by computing the transformation the phantom underwent between the independent calibration runs. This combination can be done in a post-processing step by using standard linear algebra. The method is not limited to circle-plus-arc trajectories and works for any calibration procedure in which the phantom has a preferred orientation with respect to a trajectory segment. Results are presented for both simulated as well as real data acquired with a C-arm system. We also present the first image reconstruction results for the circle-plus-arc trajectory using real C-arm data.

1. Introduction

Unlike computed tomography (CT) systems, C-arm systems are not capable of acquiring projections along an ideal trajectory because of their open design (Strobel *et al* 2003). Therefore, the trajectory has to be determined by a calibration procedure and the deviations from an ideal trajectory have to be considered in the reconstruction algorithm to avoid severe artifacts (Noo *et al* 2000, Wiesent *et al* 2000, Dennerlein *et al* 2005). The calibration procedure is consequently understood to be an obligatory step in image reconstruction in order to be able to process real data from a C-arm system. Fortunately, the C-arm motion is highly reproducible over a period of six months (Fahrig and Holdsworth 2000), and so the calibration can be done off-line with updating only needed about twice per year in clinical environments.

The term calibration here refers to the estimation of all parameters which completely describe the geometry of the cone-beam (CB) data acquisition system. Various calibration methods have been suggested in the literature (see e.g. Strobel *et al* (2003), Noo *et al* (2000), Strubel *et al* (2005), Chen *et al* (2006), Beque *et al* (2005), Yang *et al* (2006) and Smekal *et al* (2004)). For the parameter estimation, all methods require the scanning of a calibration phantom of known geometry. In the majority of cases, this phantom consists of various spheres of high attenuation which are embedded in low-attenuation base material. The measured 2D location of the spheres in the CB projection together with their known 3D positions then allows us to obtain expressions for all calibration parameters. The design of the phantom (its shape, sphere size, sphere location, number of spheres etc), however, may vary considerably and is mainly motivated by the data acquisition system, the trajectory and the object under consideration. Apart from the specific calibration phantom, the methods may be divided into two groups according to how the parameter estimation itself is done.

The first group consists of methods where the complete set of system parameters is estimated for each CB projection separately and independently of all other projections (e.g., Strobel *et al* (2003, 2005), Chen *et al* (2006)). The method in Strobel *et al* (2003) was specifically designed for C-arm image reconstruction from a circular trajectory using a calibration phantom with 108 spheres located along a spiral path. The method in Chen *et al* (2006) is similar to that in Strobel *et al* (2003); it presents a C-arm calibration procedure for a circular trajectory using a phantom with 41 spheres in a spiral arrangement. And the approach in Strubel *et al* (2005) investigates calibration for an arbitrary trajectory with a phantom consisting of 30 spheres located on three orthogonal circles and one additional sphere in the center of the phantom.

The methods belonging to the second group use more than one projection to determine the calibration parameters for each source position (e.g. Noo *et al* (2000), Beque *et al* (2005), Yang *et al* (2006) and Smekal *et al* (2004)). The method in Noo *et al* (2000) was designed to calibrate a circular trajectory by using a calibration object consisting only of two spheres. The method in Beque *et al* (2005) can be used to calibrate a pinhole camera of a single photon emission computed tomography system with a geometry similar to that of a flat-panel C-arm system. They estimate the calibration parameters using an object with three spheres. The approach in Yang *et al* (2006) investigates calibration of a CB scanner using the elliptical projection orbit of several spheres located on a planar calibration object. And (v. Smekal *et al* 2004) presents a calibration procedure for a circular trajectory based on a Fourier analysis of the projection orbit of several spheres.

This work presents a novel geometric calibration procedure for the circle-plus-arc trajectory that builds on the method in Strobel *et al* (2003). Our method is motivated by the recent development of exact reconstruction algorithms for a circle-plus-arc trajectory (Katsevich 2005, Pack and Noo 2005). This trajectory is especially well suited for C-arm systems since it can be performed purely by rotating the C-arm around the patient without the need to move the patient table. Our main idea for calibration is the separation of the trajectory into two circular segments (circle segment and arc segment) which are calibrated independently. This separation allows us to reuse the calibration phantom and the calibration procedure of (Strobel *et al* 2003), which has been successfully applied in clinical environments to calibrate the circular trajectory of numerous routinely used C-arm systems. The proposed method consists of two major steps: (i) independent calibration of the circle and the arc segment, where for each calibration run the calibration phantom is placed optimally with respect to the segment under consideration, and (ii) combination of the calibration results by computing the transformation the phantom underwent between the independent runs. The

problem of finding this transformation is formulated as a system of linear equations which is solved by using standard linear algebra.

The paper is organized as follows. After a brief review of the calibration problem for a circular trajectory in section 2, the details of the proposed calibration procedure are explained in section 3. Experiments are presented in section 4 for simulated and real CB data. Section 5 summarizes our results.

2. Background

This section defines the C-arm scanner geometry and shows how all necessary geometrical information about the device and its trajectory can be contained within projection matrices. We also provide a detailed description of the used calibration phantom together with the corresponding calibration algorithm which will later be used to calibrate each segment of the circle-plus-arc trajectory.

2.1. Mathematical notation

For the rest of the paper, we will follow the convention that vectors are per default column vectors and will appear underlined to distinguish them from scalar values, whereas matrices are assigned capital letters. Moreover, 2D points will be distinguished from 3D points by a tilde (\sim) sign, independently of the specific coordinate system they refer to. We make no distinction between homogeneous or inhomogeneous quantities, such as vectors or matrices, other than giving textual guidance where this is necessary. Thus, a 3D point \underline{x} will either have dimension 4×1 or 3×1 and a 2D point $\tilde{\underline{x}}$ will have dimension 3×1 or 2×1 , depending on the context. Likewise, equations involving homogeneous quantities are treated as normal equations using an equal ($=$) sign. The equal sign then means equal up to a non-zero scaling factor, since each side of the equation may be multiplied by such a factor without changing the equation.

2.2. Scanner geometry

In C-arm CT, the projective geometry can be described by assigning to each measurement position one homogeneous 3×4 matrix P that contains all geometrical information about the measurement (Hartley and Zisserman 2003). The matrix P is called a projection matrix because it maps a point \underline{x} from the 3D world coordinate system to a point $\tilde{\underline{x}}$ in the 2D image coordinate system according to the formula

$$\tilde{\underline{x}} = P\underline{x}, \quad (1)$$

see figure 1. Both, \underline{x} and $\tilde{\underline{x}}$ are homogeneous vectors with dimensions 4×1 and 3×1 , respectively.

The mapping described by P can be decomposed in three successive steps: (i) transformation of the point from world coordinates to x-ray source coordinates (Euclidian transformation); (ii) projection of the point onto the detector plane where it is represented by detector coordinates (central projection); (iii) transformation of the point to image (pixel) coordinates (affine transformation):

$$P = \underbrace{\begin{bmatrix} \frac{1}{du} & s & u_0 \\ 0 & \frac{1}{dv} & v_0 \\ 0 & 0 & 1 \end{bmatrix}}_{\text{affine transformation}} \underbrace{\begin{bmatrix} f & 0 & 0 & 0 \\ 0 & f & 0 & 0 \\ 0 & 0 & 1 & 0 \end{bmatrix}}_{\text{central projection}} \underbrace{\begin{bmatrix} R & -Ra \\ \underline{0}^\top & 1 \end{bmatrix}}_{\text{Euclidian transformation}}. \quad (2)$$

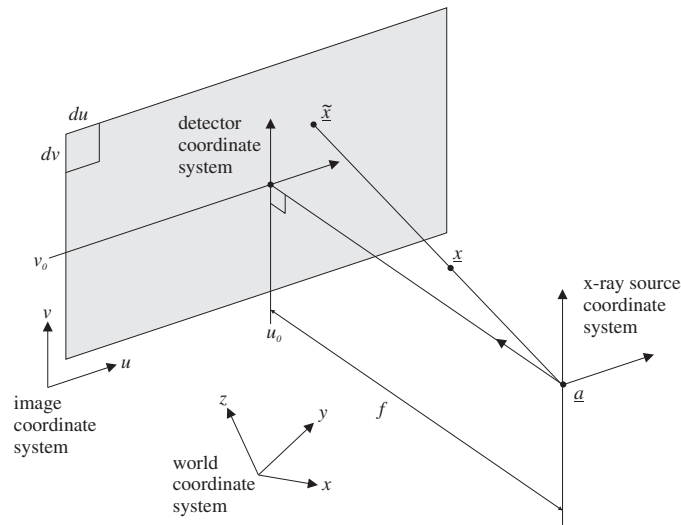


Figure 1. A projection matrix describes the mapping of any point \underline{x} from 3D world coordinates to 2D image coordinates $\tilde{\underline{x}}$ and thus contains all geometrical information about the C-arm device for a given CB projection.

In this decomposition, R is an inhomogeneous 3×3 rotation matrix giving the detector orientation, \underline{a} is an inhomogeneous 3×1 vector describing the x-ray source position in the world coordinate system, f is the focus-to-detector distance, du is the pixel width, dv is the pixel height, s is known as the ‘skew’ parameter because a value of s other than zero amounts to a device with a sheared detector pixel grid, and $(u_0, v_0)^\top$ are the coordinates of the orthogonal projection of the source position onto the detector plane. These coordinates are in the image coordinate system, the origin $(0, 0)^\top$ of which was chosen to be at the lower left corner of the image, though a different choice could have been made just as well.

2.3. Calibration phantom

A CB projection of the calibration phantom at a given source–detector position typically allows the determination of the projection matrix P for this position. For this determination, which will be further discussed in section 2.4, it is required that the geometrical shape of the calibration phantom is exactly known in the world coordinate system. The world coordinate system is thereby attached to the phantom. Thus, a different phantom location or orientation defines a different world coordinate system. Often, the phantom consists of various spheres of high attenuation which are distributed over a control region of predefined extent and which are enclosed in low-attenuation base material. In this work, we use the PDS-2 calibration phantom (Siemens AG, Medical Solutions, Forchheim, Germany) as in Strobel *et al* (2003) (see figure 2). This phantom was originally designed to calibrate a trajectory consisting of a circle or partial circle. It consists of a cylindrical wall made of low-attenuation material. Its outer radius is 72 mm and its inner radius is 62 mm measured from the symmetry axis of the phantom. The height of the cylinder is 206 mm. Inside the wall, there are 108 spheres made of noncorrosive steel with two different radii arranged along a spiral-shaped path. The large spheres have a diameter of 3.2 mm and the small spheres have a diameter of 1.6 mm. The sequence of alternating large and small spheres represents a binary string

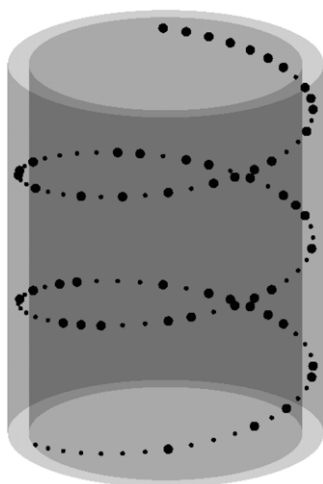


Figure 2. The PDS-2 calibration phantom contains 108 steel spheres. The big spheres constitute a logical 1 and the small spheres constitute a logical 0.

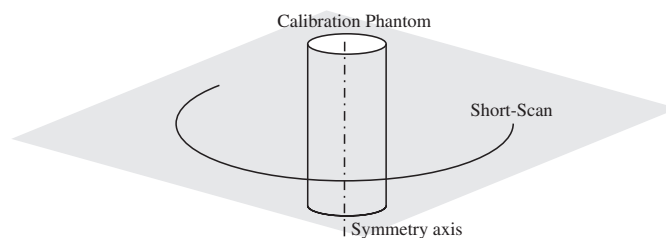


Figure 3. The optimal phantom placement for a short-scan circular trajectory is shown. The phantom is placed near the iso-center of the scan with its main symmetry axis parallel to the rotation axis.

with an 8 bit encoding, such that an arbitrary subsequence of length 8 provides enough information to identify each sphere of the sequence uniquely within the whole binary string. This identification is independent of any associated coordinate system since only the bit sequence is relevant here. In fact, this property is used to establish unique correspondences between the 2D images of the spheres in the CB projection and their 3D counterparts.

We would like to note that the dimensions of the phantom as well as the size of the spheres assume a C-arm geometry which is similar to that of the scanner we used in our experiments. Other geometries may lead to different magnification factors so that the phantom may not be completely within the scanner field of view. Therefore, in order to utilize a scanner with very different source–object–detector distances, it may become necessary to adapt the phantom accordingly.

2.4. Calibration algorithm

To calibrate a circular short-scan or full-scan trajectory, the PDS-2 phantom is placed near the iso-center of the scan with its main symmetry axis almost parallel to the rotation axis (see figure 3). This arrangement guarantees that the projection of the spheres are arranged along an ‘S-curve’ in every CB image acquired along the trajectory. Otherwise, when the phantom

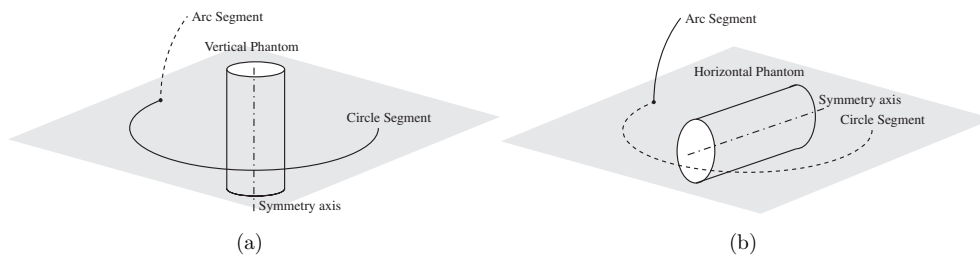


Figure 4. The optimal phantom placement for the circle-plus-arc trajectory for (a) the circle and (b) the arc segment is shown. Here, the phantom placement to calibrate the arc segment differs from that of the circle segment by a 90° rotation.

is observed from oblique viewing directions, spheres may overlap in the projection and the projected spiral may cross over itself, so that the task of locating and ordering the spheres becomes challenging and thus impractical. Locating and ordering the spheres however is an important part of the calibration algorithm, which proceeds in four major steps: (i) localization of the spheres in the image, (ii) ordering of the located spheres, (iii) establishment of unique correspondence between the projection of the spheres in the images and their 3D counterparts by decoding binary substrings of length 8, and (iv) estimation of the projection matrix for each source position. See Strobel *et al* (2003) for details on the last step. Once the algorithm has at least found a sequence of eight spheres for the decoding step, an initial estimate of the projection matrix can be computed. Additional spheres can be located in the image by projecting all spheres onto the image plane using the estimated projection matrix, and then performing a neighbor search around the projection of previously unlocated spheres. The process is repeated until no more spheres can be found.

3. Calibration of the circle-plus-arc trajectory

The calibration algorithm explained in section 2.4 is well suited to calibrate each circular segment of the circle-plus-arc trajectory. For that task, the PDS-2 calibration phantom needs to be positioned separately for each segment. As motivated before, its main symmetry axis should be oriented almost parallel to the rotation axis of the segment under consideration (see figure 4). As a consequence of a non-optimal phantom placement, only a part of the trajectory may be calibrated, if any. Indeed it will be seen in section 4, that no more than the first 12° of the arc segment could be reliably calibrated with the phantom in the position associated with the circular scan (the vertical phantom of figure 4(a)). However, the arc length required to obtain complete data for reconstruction is typically of 22° .

When placing the phantom differently from one segment of the trajectory to the other, one encounters the problem that the projection matrices obtained for the segments refer to different world coordinate systems and have to be registered such that they refer to a single common world coordinate system. We have developed a method to achieve this registration, providing thereby a way to calibrate the circle-plus-arc trajectory as a whole, using optimal placement of the phantom for each of its segments. The registration was done by the determination of the change in position and orientation applied to the phantom from calibration of the first segment to the next one, using information provided by so-called connection points (CPs). The term connection point refers to any source position for which two projection matrices can be obtained—one using the vertical and the other one using the horizontal phantom placement. From a theoretical point of view, when the phantom is moved from one location to another,

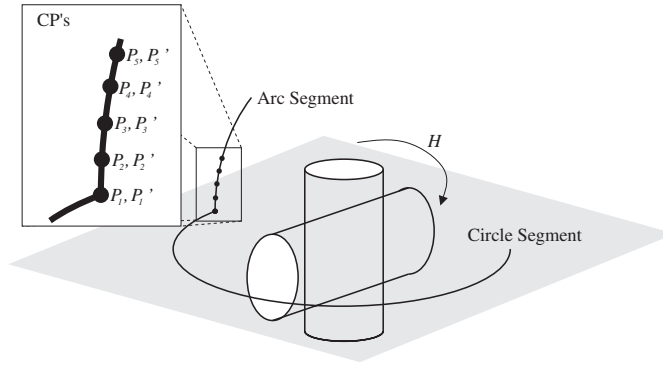


Figure 5. Connection points along the arc segment. As the name implies, they provide a connection between the vertical and the horizontal phantom placement which can be used to compute the phantom motion.

one CP will suffice to determine the phantom motion. Therefore, we will first describe the theory using a single CP and then extend the results using many CPs.

3.1. Calibration using one connection point

We choose our CP to be one of those depicted in figure 5, located on the arc segment. Assume we have determined the projection matrices P and P' for this CP by applying the calibration procedure of section 2.4 first on the vertical phantom to get P and then on the horizontal phantom to get P' . Two arbitrary projection matrices can always be transformed into each other by multiplying either of them by a homogeneous 4×4 matrix, say H , as follows (Hartley and Zisserman 2003):

$$P = P'H. \quad (3)$$

The matrix H is called a homography and has 15 degrees of freedom which results from its 16 entries minus one because a multiplication of H with an arbitrary non-zero scaling factor does not change the transformation implied. Because only the position of the phantom changed from the calibration of P to P' , H describes the motion the phantom experienced thereby. Once H is known, equation (3) can be used to transform the projection matrix P' into P at all x-ray source positions along the arc segment, especially where only P' is available, so that finally the projection matrices of the arc segment refer to the same world coordinate system as those of the circle segment.

To obtain H , we choose a set of 3D points \underline{x}_i expressed in the world coordinate system defined by P . Because $P = P'H$, the matrix P will project the points \underline{x}_i to the same locations as the matrix $P'H$. We may therefore write

$$P\underline{x}_i = P'H\underline{x}_i. \quad (4)$$

It is obvious that equation (4) is linear in the unknown entries of H . By ordering these entries row-wise into a 16×1 vector \underline{h} , we can reformulate (4) such that after some calculation which is shown in appendix A, we obtain

$$A_i \underline{h} = \underline{0}, \quad (5)$$

where A_i has dimension 2×16 . We call A_i the measurement matrix because it is made up only of known quantities P , P' , \underline{x}_i . Because \underline{h} has 16 entries and 15 degrees of freedom, we need 15 linearly independent equations to solve for \underline{h} . Since each point \underline{x}_i provides two equations

in the form of (5), a minimum of $n = 8$ points allow us to determine \underline{h} . More rigorously, for a minimal configuration, one can set up 14 equations from the first seven points and then add one of the two equations of the remaining eighth point. However, in the case of errors in P or P' it is recommended to use more than eight points to provide a stable estimate for \underline{h} . In that case, the A_i resulting from each point x_i will be stacked on top of each other to generate a composed measurement matrix B of dimension $2n \times 16$, with

$$B\underline{h} = \underline{0}, \quad (6)$$

where

$$B = \begin{bmatrix} A_1 \\ A_2 \\ \vdots \\ A_n \end{bmatrix}. \quad (7)$$

If $n \geq 8$ and if the measurements are not exact, e.g. P or P' are not error-free, equation (6) will only be satisfied approximately. Therefore, we define the solution \underline{h} as the vector of norm 1 that minimizes $\|B\underline{h}\|$. Numerically, this solution can be calculated as the right-hand singular vector corresponding to the smallest singular value of B by using a singular value decomposition, as suggested in Hartley and Zisserman (2003) for similar problems. This basically corresponds to a linear least-squares estimation of H .

There exist a number of so-called degenerate configurations which involve the distribution of the points x_i as well as the location of the CP under consideration, where no unique solution for H can be obtained. These degenerate configurations are independent of errors in P or P' and can occur even if both P and P' are error-free (for further reading we refer to (Hartley and Zisserman 2003), see in particular chapter 22). In short terms, we can say that the points x_i may be chosen arbitrarily as long as they are well distributed inside the field of view. Especially, the points must not be coplanar or otherwise lie on a linear subspace of \mathbb{R}^3 . Also, the uniqueness of H strongly depends on the location of the chosen CP. Even close-to-degenerate locations must be avoided. For example, the very first CP of figure 5, located at the connection of circle and arc segment, causes a degenerate configuration if the phantom is rotated according to figure 4, no matter how the points x_i are distributed. This is so because in this case one can show that P and P' are related via a 3×3 homographic matrix, say J , such that $P = JP'$. Because J has nine entries but only 8 degrees of freedom, the relation between P and P' lets us determine only eight free parameters. Consequently, there are $15 - 8 = 7$ parameters in H that are not uniquely defined by B . Therefore, in practice, it might be useful to look at the singular values of B . If the smallest singular values have the same magnitude, we may assume that B is not well conditioned and that the solution might be unstable. We investigated this and found that the situation becomes fundamentally different when incorporating more than one CP. Just how many CPs are needed is shown in section 4, where we plot the error associated with H over a varying number of CPs.

3.2. Calibration using many connection points

For improved stability, we want to incorporate more than one CP, e.g. all CPs depicted in figure 5. This can be done in a straightforward manner given the theory of the last section. From each connection point CP_j , with $j = 1, \dots, k$, a $2n \times 16$ measurement matrix B_j is obtained. Again, the B_j will be stacked on top of each other resulting in a composed measurement matrix C of size $2nk \times 16$, with

$$C\underline{h} = \underline{0}, \quad (8)$$

Table 1. Parameters used for the experiments.

	Simulated CB data	Real CB data
Radius (circle/arc) (mm)	750	750
Focus-to-detector distance (f) (mm)	1200	1200
Pixel width (du) (mm/px)	0.372	0.372
Pixel height (dv) (mm/px)	0.372	0.372
Detector dimension (px ²)	1024 × 1024	1024 × 1024
Angular sampling (circle) (°/projection)	0.4	0.4
Angular sampling (arc) (°/projection)	0.4	0.4
Number of projections (circle)	538 (214.8°)	538 (214.8°)
Number of projections (arc)	50 (19.6°)	50 (19.6°)

where

$$C = \begin{bmatrix} B_1 \\ B_2 \\ \vdots \\ B_k \end{bmatrix}. \quad (9)$$

As before, the solution \underline{h} is obtained as the vector of norm 1 that minimizes $\|C\underline{h}\|$.

4. Experiments

Experiments were performed using simulated as well as real CB data acquired with a AXIOM Artis *dBA* C-arm system (Siemens AG, Medical Solutions, Forchheim, Germany). For the simulation, a detailed computer model of the calibration phantom was created. The corresponding CB projections were generated using an analytical forward projector. The phantom was rotated by 90° according to figure 4 but in addition translated by 10 mm along the z -axis to mimic a realistic phantom motion. The parameters of the experiments are given in table 1. For the computation of H , we chose the \underline{x}_i to be the midpoints of the spheres of the calibration phantom because they are well distributed over the field of view. Since the phantom has 108 spheres, this gives $n = 108$ points.

In order to measure how well H has been estimated, we computed the root-mean-square (RMS) error between the true and registered projection matrices P^* and $P'H$ for each source position along the arc segment according to

$$\sigma = \left(\frac{1}{m} \sum_{i=1}^m (P^* \underline{y}_i - P'H \underline{y}_i)^2 \right)^{1/2}. \quad (10)$$

Here, the 3D points \underline{y}_i are homogeneous 4×1 vectors and P^* is the error-free version of P . Note that both homogeneous 3×1 vectors $P^* \underline{y}_i$ and $P'H \underline{y}_i$ must be inhomogenized by dividing each vector by its last component before applying the equation to compute σ . Also note that σ is measured in pixel (px) units because $P^* \underline{y}_i$ and $P'H \underline{y}_i$ represent points in the image coordinate system. The points \underline{y}_i were chosen to lie on a square grid with a 5 mm sampling. We performed experiments with two different point sets (see figure 6). The first set S_1 was located inside a cylinder of radius $r_1 = 70$ mm and height $h = 140$ mm (which corresponds to the control region defined by the calibration phantom), such that $S_1 = \{ \underline{y}_i = (x_i, y_i, z_i, 1)^T \mid x_i^2 + y_i^2 \leq r_1^2 \cap -h/2 \leq z_i \leq h/2 \}$. This selection resulted in $m = 17\,777$ points. The second set S_2 was located outside this cylinder (to see what happens beyond the control region) and bounded by the scanner field of view with $r_2 = 125$ mm,

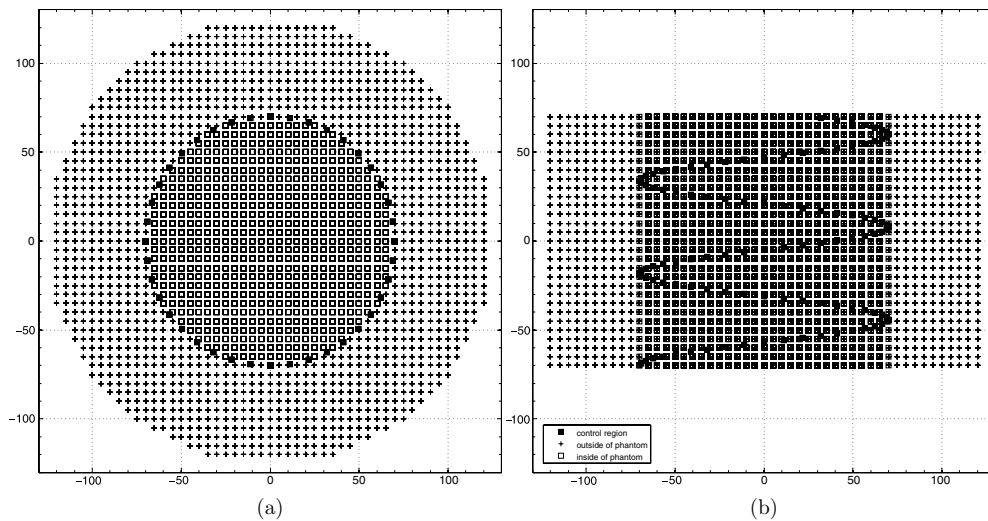


Figure 6. The points y_i used to compute the RMS error are evenly distributed inside and outside the control region defined by the midpoints x_i of the steel spheres of the calibration phantom. (a) Orthogonal projection of these points onto the xy -plane. (b) Orthogonal projection onto the xz -plane.

with $S_2 = \{y_i = (x_i, y_i, z_i, 1)^T \mid x_i^2 + y_i^2 > r_1^2 \cap x_i^2 + y_i^2 \leq r_2^2 \cap -h/2 \leq z_i \leq h/2\}$ and $m = 38\,976$. Thus, both point sets differ in number and position from the points x_i used to compute H .

The RMS error for both point sets is shown in figure 7 for simulated and real CB data. For the simulated data, we were able to calibrate P with the vertical phantom on the first 28 source positions along the arc segment, measured from the connected end of the arc. The projection matrix P' was calibrated from the horizontal phantom for all 50 source positions on the arc. Thus, H was estimated from the CPs related to the first 28 source positions where we have both P and P' . This corresponds to an arc length of 10° . Since we have simulated data, the ground truth P^* was available for all source positions, even beyond the last connection point.

The situation becomes different for the real data. Here, we were able to calibrate P on the first 31 source positions and P' on all 50 source positions as before. This resulted in 31 CPs along the arc corresponding to an arc length of 12° . However, for real data we don't know the ground truth P^* and so we used P instead of P^* to evaluate the RMS error. This is why the plot stops at position 31. Since P is also needed to estimate H , we dropped every second CP and computed H only from the remaining 16 CPs to obtain a value for σ which is more independent of the calibration. The fact that we have a different number of CPs for simulated and real data is caused by a slightly different phantom position in both cases.

The RMS error gives an estimate of how much the average projected point deviates from its true position. A different error measurement may be chosen instead. For example, (Faugeras 1996) suggests a decomposition of the projection matrices to obtain every single calibration parameter e.g. x-ray source position, focus-to-detector distance, skew etc. However, by comparing these values separately, we get only little insight into how accurately the point mapping itself behaves, because deviations from different measurements may compensate for each other when acting together on a point in 3D space. With regard to image reconstruction, we need an error measurement which we expect to correlate well with the errors in the backprojection step of the reconstruction algorithm, since this is the step we care about the

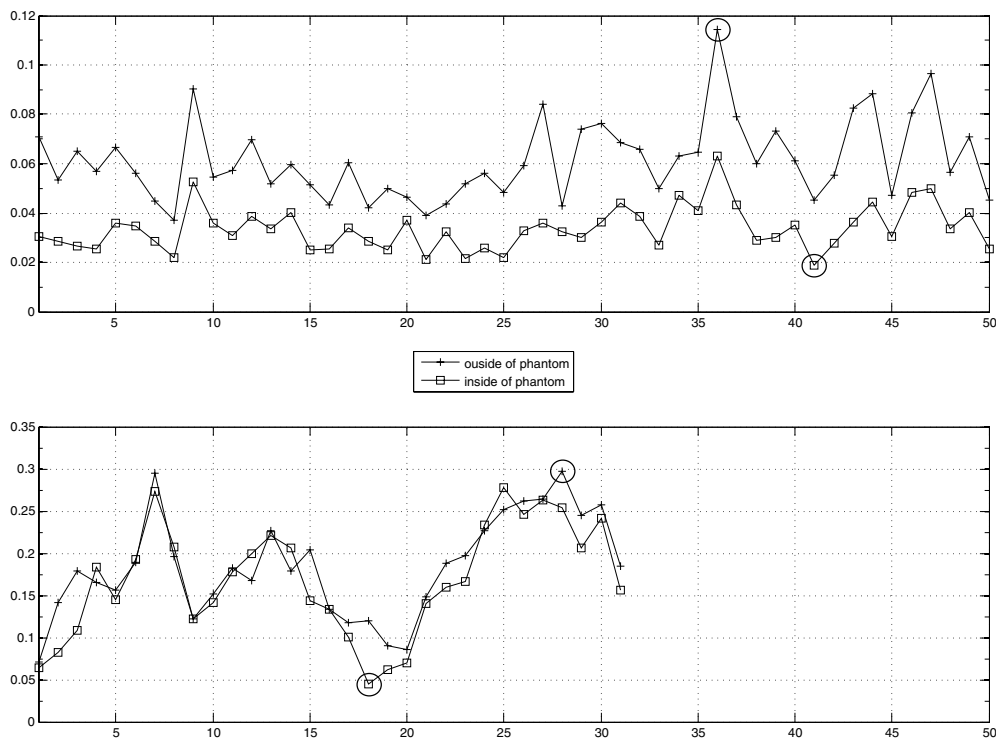


Figure 7. Calibration accuracy from simulated (top) and real CB data (bottom) for the calibrated arc segment. In each case, the projection number is plotted against the RMS error given in pixel units. Projection 50 corresponds to the last source position (at 19.6°) along the arc segment. The minimal and maximal overall errors (marked with circles) are 0.019 px (projection 41) respectively 0.114 px (projection 36) for simulated and 0.045 px (projection 18) and 0.297 px (projection 28) for real data, respectively.

most. For this reason, we prefer to use (10) instead of the measure suggested in Faugeras (1996).

From the figure it is observed that our approach achieves sub-pixel accuracy even with real data. For simulated data, we see that the error is higher for points outside the phantom as for those inside, as expected. Still, the error is far below one pixel. The accuracy of real data is reduced by a factor of 3 compared to simulated data. Also, in contrast to simulated data, no significant error difference can be observed between the two point sets for real data. We believe that both effects are a consequence of using a real data acquisition system. For example, the fact that the error difference for points inside and outside the phantom is small may be due to the ground truth being known only approximately. Further on, we assume that the higher errors for real data compared to simulated data are coming from inaccuracies of the underlying calibration procedure (sphere localization etc). However, it is quite possible that physical phenomena such as quantum noise or beam hardening also play a role.

Figure 8 shows the projection of the midpoints \underline{x}_i of the steel spheres of the calibration phantom onto the acquired projection images for simulated and real CB data, respectively. Those points were projected with the projection matrices which are associated with the minimal and maximal RMS errors (cf figure 7). We included this figure for three reasons. First, to provide an illustration of the calibration results. Second, to see how the CB projections of the

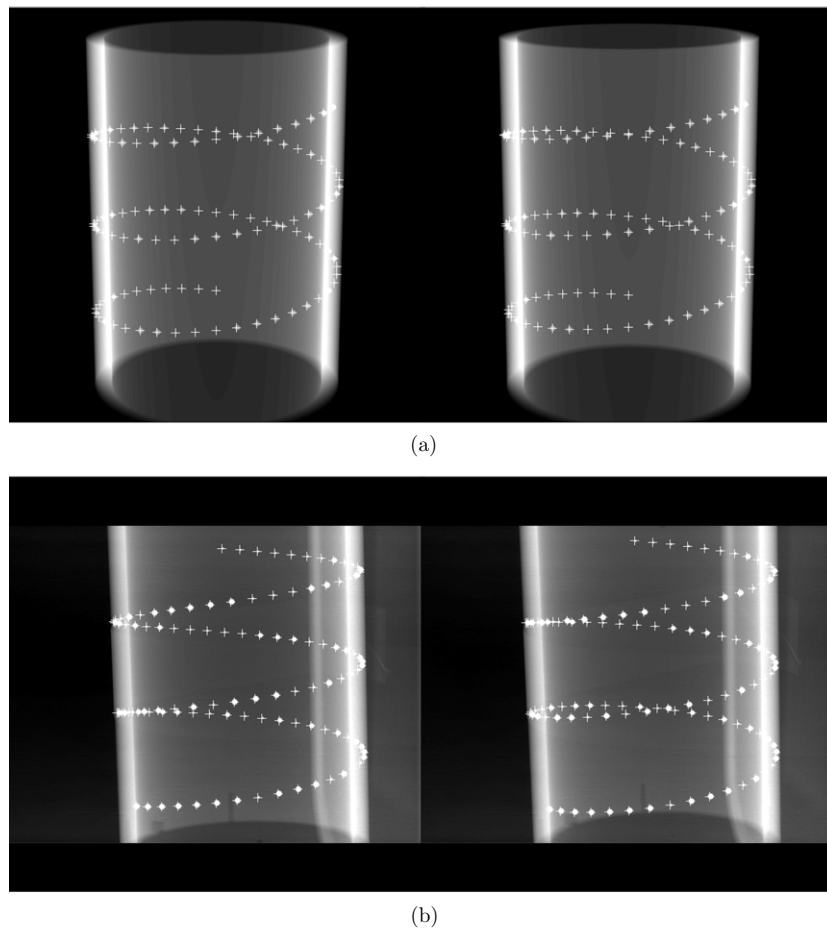


Figure 8. Projection of all 108 midpoints (indicated by white crosses) of the steel spheres of the calibration phantom onto (a) the simulated and (b) the real CB data from source positions corresponding to the minimal (left) and maximal RMS errors (right). Note that the white crosses do not belong to the CB projections but were inserted only to demonstrate the calibration results.

calibration phantom look like, especially for real data and third, to demonstrate qualitatively that the simulated data and the real data are very similar.

In figure 9, the maximal RMS error is plotted over a varying number of CPs. For simulated data, H was computed from 1, 2, ..., 28 CPs in turn, starting from the end of the arc segment connected to the circle segment. Each time, the error was computed for all 50 source positions using P^* and the maximal value thereof is shown. For real data, we computed H from 1, 2, ..., 31 CPs and evaluated the error on 31 source positions using P as the ground truth as above. In each case, the points \underline{y}_i were located inside the control region of the phantom. The figure shows that the error is quite high for a single CP. As explained earlier, this CP (located at the connection of circle and arc segment) leads to a degenerate configuration when the phantom is rotated according to figure 4 (we further discuss this in section 5). However, as soon as more CPs are involved, the ambiguities in estimating H are resolved and the error drops rapidly below one pixel, starting from the third (simulated data) respectively the fifth CP (real data), and then levels off gradually until the improvements are negligible. Another

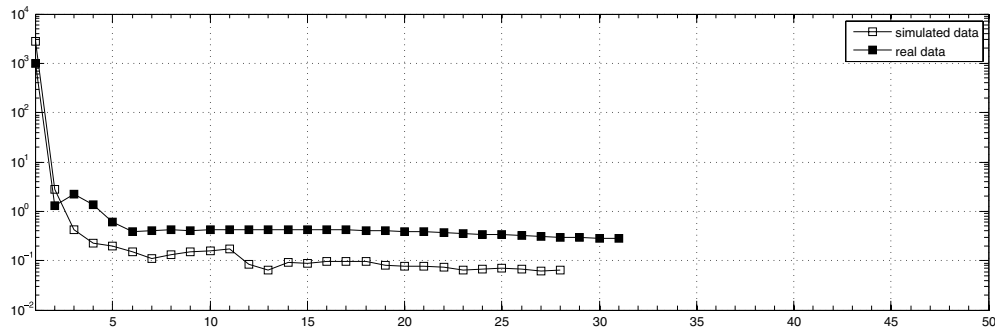


Figure 9. Maximal RMS error over a varying number of CPs for simulated and real CB data. The error is plotted using a logarithmic scale.

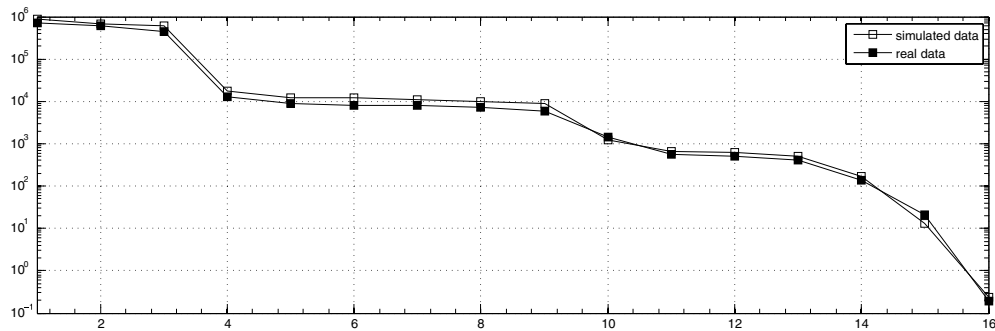


Figure 10. Singular values $s_1 \dots s_{16}$ of the composed measurement matrix C for simulated and real CB data. The singular values are plotted in descending order using a logarithmic scale.

observation is that some CPs lead to higher errors when added, see for example the curve progression from 13 to 14 (simulated data) or from 2 to 3 (real data). Thus, the RMS error may provide a means for singling out ‘bad’ CPs should this become necessary.

Figure 10 shows the singular values $s_1 \dots s_{16}$ of the composed measurement matrix C with dimension $2nk \times 16$ for the simulated ($n = 108, k = 28$) and the real ($n = 108, k = 16$) experiment. A few observations: (i) The plots for simulated and real data are almost identical. (ii) Singular value s_{16} differs from s_{15} by a factor of magnitude 10^2 , while any other two successors differ by a factor of magnitude 10 or less. (iii) The difference between s_1 and s_{16} is in the order of 10^7 . From (i), we see that the simulated and the real data set have the same numerical characteristics. Thus, with our simulation, the numerical behavior of a real system appears to be reproducible. From (ii) and (iii), we observe that the matrix C has a very large condition number $c = s_1/s_{16}$ and therefore seems to be singular with s_{16} being considerably smaller than all other singular values, as it should be. The fact that s_{16} is close to but not exactly equal to zero, can be attributed to measurement errors in P or P' (e.g., resulting from the sphere localization of the underlying calibration procedure).

Figure 11 shows reconstructions of a modified clock phantom (Turbell 2001), see appendix B, using the M -line approach according to (Hoppe *et al* 2006). The simulation of the phantom was done with the geometry of table 1 for simulated CB data. In addition to the modifications, the phantom was also shifted by 100 mm along the z -axis such that the slices shown in the figure at $z = 100$ mm required about 44 of the 50 projections along the arc segment for accurate reconstruction. This corresponds to 88% of the projections of the arc segment. For

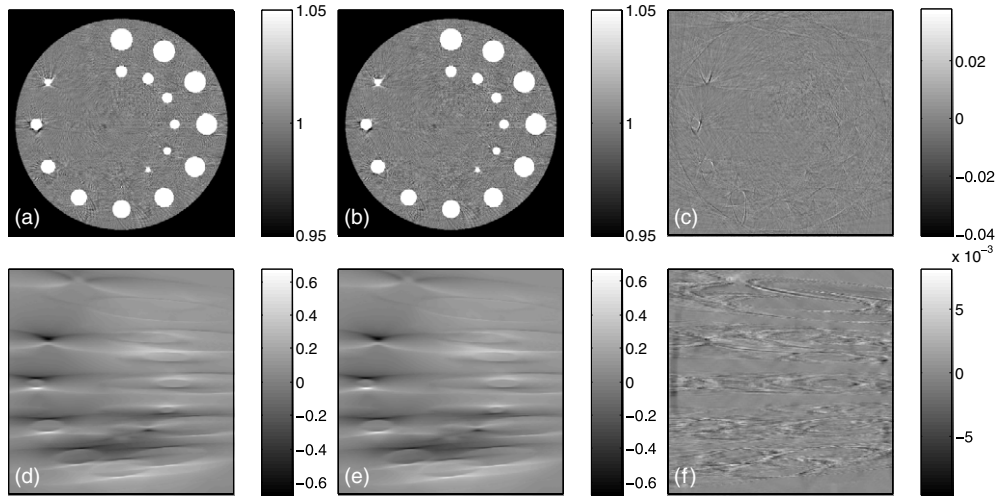


Figure 11. The slice at $z = 100$ mm through the modified clock phantom. In (a), we used the ground truth P^* for both, the circle and the arc segment. In (b), we used only calibrated quantities, that is the calibrated projection matrices P for the circle segment and the registered projection matrices $P'H$ for the arc segment. (c) Difference image: (a) minus (b). (d) Arc contribution of (a). (e) Arc contribution of (b). (f) Difference image: (d) minus (e).

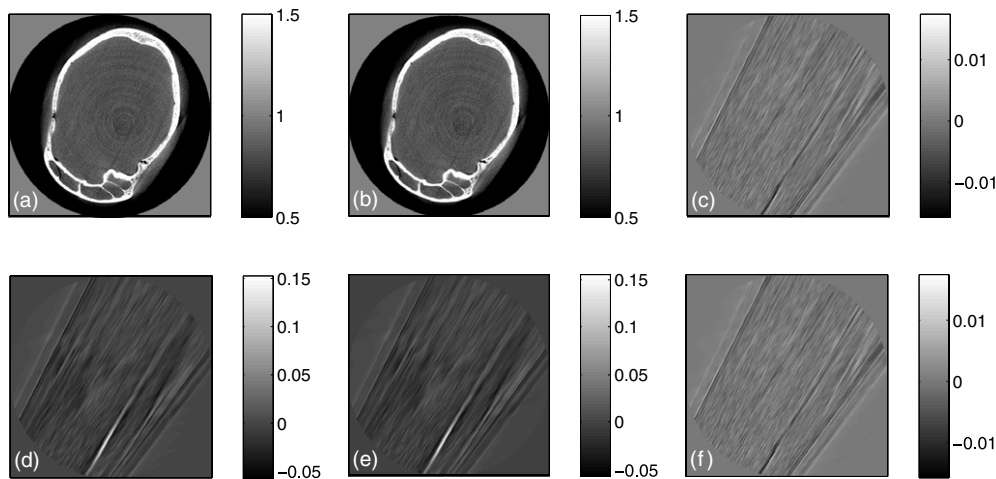


Figure 12. The slice at $z = 30$ mm through the human head phantom. In (a), we used the calibrated projection matrices P for both, the circle and the arc segment. In (b), we used the same projection matrices for the circle as in (a) but we replaced the projection matrices of the arc segment by the registered projection matrices $P'H$. (c) Difference image: (a) minus (b). (d) Arc contribution of (a). (e) Arc contribution of (b). (f) Difference image: (d) minus (e).

calibration, all 28 CPs along the arc were used to compute the matrix H . Thus in (b) and (e), the reconstruction algorithm used 16 projections beyond the last CP which were not part of the estimation of H . From (c), we see that differences between the reconstruction using P^* and the one using P (for the circle) and $P'H$ (for the arc) are visible mainly for the two smallest spheres on the outer ring. With increasing sphere size, those differences become negligible. From (f), we see that both arc contributions are almost identical.

Figure 12 shows M -line reconstructions of a human head phantom. The CB data were acquired with the AXIOM Artis dBA C-arm system (Siemens AG, Medical Solutions, Forchheim, Germany) specified as in table 1 for real CB data. Note that no pre- or post-processing steps were applied to the data other than logarithmic scaling. For the calibration of the system, all 31 CPs were used to compute the matrix H . The reconstructed slice at $z = 30$ mm was chosen such that less than 31 projections along the arc segment were required for accurate reconstruction to allow a comparison between reconstructions using the calibrated projection matrices P (which here again act as our ground truth) and the registered projection matrices $P'H$. As can be seen from (c) and (f), the differences between the reconstruction using P and the one using $P'H$ are marginal. The fact that (c) and (f) are almost identical can be explained from the circle contributions of (a) and (b) being almost the same (except for the backprojection weighting masks which are determined by the arc segments, cf Hoppe *et al* (2006)). Therefore, the arc contributions define the appearance of the difference images.

5. Discussion and conclusions

We have presented a method to calibrate the circle-plus-arc trajectory. The method consists of two steps: (i) independent calibration of the circle and the arc segment by placing the calibration phantom optimally for each segment, and (ii) combination of the calibration results by computing the transformation the phantom underwent between the independent runs. The first step built on an accurate and robust calibration procedure for circular trajectories. The second step presented new material. The idea of combining different trajectory segments by identifying the phantom motion applies to any calibration procedure in which the calibration phantom has a favored orientation with respect to a trajectory segment.

It has been shown that the phantom motion can be computed from so-called connection points along the arc segment using standard linear algebra. Experiments for simulated and real CB data have demonstrated that the method works with sub-pixel accuracy at least for our specific C-arm device, if five or more connection points are provided. Other scanners and scanner geometries might require a different number of connection points though this has not been evaluated. Our calibration results have been confirmed with reconstructions of a modified clock phantom using computer-simulated CB data and of a human head phantom using real CB data. To our knowledge, image reconstructions for the circle-plus-arc trajectory using real C-arm data have not been published before.

In addition to the experiments corresponding to figure 9, we have also attempted to calibrate the system from only one connection point trying different locations along the arc segment. We used every available connection point in turn and found consistently that no better results could be obtained by using a single connection point only, no matter which one, than those already shown and so these results have been omitted.

Often, the circle-plus-arc trajectory is two sided, which means that two arc segments (arc-up and arc-down) are attached to the circle segment to allow reconstruction above and below the circle plane. Depending on the location of the two arc segments relative to each other, the trajectory can be calibrated in one of the two ways. Whenever the two arc segments can be calibrated from one and the same phantom position (for example, because the arcs are connected to each other at their end points), the connection points of the two arc segments can be combined into a single measurement matrix and the computation of the phantom motion can be done as if there had only been one arc segment. Then, both arcs are transformed into the coordinate system of the circle segment using the computed phantom motion. When the phantom has to be placed differently for each arc segment (for example because the arcs are attached at different end points of the circle segment), the whole calibration procedure must

be performed twice, calibrating first the circle-plus-arc-up and then the circle-plus-arc-down trajectory such that afterwards, both arcs refer to the coordinate system of the shared circle segment.

Acknowledgments

This work was supported by Siemens AG, Medical Solutions and was supported in part by the U.S. National Institutes of Health (NIH) under grant R01 EB000627.

Appendix A. Determination of the measurement matrix

In this appendix, we show how the entries of the measurement matrix A_i can be determined, following steps similar to Hartley and Zisserman (2003). Our starting point is equation (4), section 3.1,

$$P\underline{x}_i = P'H\underline{x}_i. \quad (\text{A.1})$$

We proceed by applying the vector cross product to obtain

$$P\underline{x}_i \times P'H\underline{x}_i = \underline{0}. \quad (\text{A.2})$$

We denote the j th row of the matrix P' by $\underline{p}^{j\top}$ and the j th column of the matrix H by \underline{h}_j and also $\underline{x}_i = (x_i, y_i, z_i, 1)^\top$. As an intermediate result, we find

$$P'H\underline{x}_i = \begin{pmatrix} x_i \underline{p}^{1\top} \underline{h}_1 + y_i \underline{p}^{1\top} \underline{h}_2 + z_i \underline{p}^{1\top} \underline{h}_3 + \underline{p}^{1\top} \underline{h}_4 \\ x_i \underline{p}^{2\top} \underline{h}_1 + y_i \underline{p}^{2\top} \underline{h}_2 + z_i \underline{p}^{2\top} \underline{h}_3 + \underline{p}^{2\top} \underline{h}_4 \\ x_i \underline{p}^{3\top} \underline{h}_1 + y_i \underline{p}^{3\top} \underline{h}_2 + z_i \underline{p}^{3\top} \underline{h}_3 + \underline{p}^{3\top} \underline{h}_4 \end{pmatrix}. \quad (\text{A.3})$$

Now the cross product can be written as

$$P\underline{x}_i \times P'H\underline{x}_i = \begin{pmatrix} x_i \underline{a}^\top \underline{h}_1 + y_i \underline{a}^\top \underline{h}_2 + z_i \underline{a}^\top \underline{h}_3 + \underline{a}^\top \underline{h}_4 \\ x_i \underline{b}^\top \underline{h}_1 + y_i \underline{b}^\top \underline{h}_2 + z_i \underline{b}^\top \underline{h}_3 + \underline{b}^\top \underline{h}_4 \\ x_i \underline{c}^\top \underline{h}_1 + y_i \underline{c}^\top \underline{h}_2 + z_i \underline{c}^\top \underline{h}_3 + \underline{c}^\top \underline{h}_4 \end{pmatrix} = \underline{0}, \quad (\text{A.4})$$

with

$$\underline{a} = (\underline{p}^{2\top} \underline{x}_i) \underline{p}^3 - (\underline{p}^{3\top} \underline{x}_i) \underline{p}^2 \quad (\text{A.5})$$

$$\underline{b} = (\underline{p}^{3\top} \underline{x}_i) \underline{p}^1 - (\underline{p}^{1\top} \underline{x}_i) \underline{p}^3 \quad (\text{A.6})$$

$$\underline{c} = (\underline{p}^{1\top} \underline{x}_i) \underline{p}^2 - (\underline{p}^{2\top} \underline{x}_i) \underline{p}^1, \quad (\text{A.7})$$

where $\underline{p}^{j\top}$ is the j th row of P . Equivalently,

$$P\underline{x}_i \times P'H\underline{x}_i = \begin{bmatrix} x_i \underline{a}^\top & y_i \underline{a}^\top & z_i \underline{a}^\top & \underline{a}^\top \\ x_i \underline{b}^\top & y_i \underline{b}^\top & z_i \underline{b}^\top & \underline{b}^\top \\ x_i \underline{c}^\top & y_i \underline{c}^\top & z_i \underline{c}^\top & \underline{c}^\top \end{bmatrix} \begin{pmatrix} \underline{h}_1 \\ \underline{h}_2 \\ \underline{h}_3 \\ \underline{h}_4 \end{pmatrix} = \underline{0}. \quad (\text{A.8})$$

This is a system of three equations. However, in general, the vector \underline{c} is a linear combination of the vectors \underline{a} and \underline{b} and so the third equation does not provide much additional information if any, even if P or P' are not error-free. We therefore decided to use only the first two equations.

Thus, we obtain

$$A_i = \begin{bmatrix} x_i \underline{a}^\top & y_i \underline{a}^\top & z_i \underline{a}^\top & \underline{a}^\top \\ x_i \underline{b}^\top & y_i \underline{b}^\top & z_i \underline{b}^\top & \underline{b}^\top \end{bmatrix}, \quad (\text{A.9})$$

with \underline{a} and \underline{b} as defined above.

Table B1. The midpoints $(m_x, m_y, m_z)^\top$, radii $(e_x, e_y, e_z)^\top$ and densities ρ of the spheres of the modified clock phantom. For the water cylinder in the first row, e_x (respectively e_y) gives its radius and e_z its half-height.

m_x (cm)	m_y (cm)	m_z (cm)	e_x (cm)	e_y (cm)	e_z (cm)	ρ (HU/1000+1)
0.00	0.00	0.00	8.00	8.00	2.40	1.00
0.00	6.40	0.00	0.80	0.80	0.80	2.00
3.20	5.52	0.08	0.80	0.80	0.80	2.00
5.52	3.20	0.16	0.80	0.80	0.80	2.00
6.40	0.00	0.24	0.80	0.80	0.80	2.00
5.52	-3.20	0.32	0.80	0.80	0.80	2.00
3.20	-5.52	0.40	0.80	0.80	0.80	2.00
0.00	-6.40	0.48	0.80	0.80	0.80	2.00
-3.20	-5.52	0.56	0.80	0.80	0.80	2.00
-5.52	-3.20	0.64	0.80	0.80	0.80	2.00
-6.40	0.00	0.72	0.80	0.80	0.80	2.00
-5.52	3.20	0.80	0.80	0.80	0.80	2.00
-3.20	5.52	0.88	0.80	0.80	0.80	2.00
0.00	4.00	0.00	0.40	0.40	0.40	2.00
2.00	3.44	-0.08	0.40	0.40	0.40	2.00
3.44	2.00	-0.16	0.40	0.40	0.40	2.00
4.00	0.00	-0.24	0.40	0.40	0.40	2.00
3.44	-2.00	-0.32	0.40	0.40	0.40	2.00
2.00	-3.44	-0.40	0.40	0.40	0.40	2.00
0.00	-4.00	-0.48	0.40	0.40	0.40	2.00
-2.00	-3.44	-0.56	0.40	0.40	0.40	2.00
-3.44	-2.00	-0.64	0.40	0.40	0.40	2.00
-4.00	0.00	-0.72	0.40	0.40	0.40	2.00
-3.44	2.00	-0.80	0.40	0.40	0.40	2.00
-2.00	3.44	-0.88	0.40	0.40	0.40	2.00

Appendix B. Modified clock phantom

Table B1 shows our version of the clock phantom originally presented in Turbell (2001). Compared to the definition given in Turbell (2001), the phantom has been scaled by a factor of 8, the densities of the spheres have been raised from 0 HU to 1000 HU and the spheres have been embedded in a surrounding water cylinder.

References

- Beque D, Nuyts J, Suetens P and Bormans G 2005 Optimization of geometrical calibration in pinhole spect *IEEE Trans. Med. Imaging* **24** 180–90
- Chen G, Zambelli J, Nett B, Supanich M, Riddell C, Belanger B and Mistretta C 2006 Design and development of C-arm based cone-beam CT for image-guided interventions: initial results *Proc. SPIE* **6142** 336–47 doi:10.1117/12.653197
- Dennerlein F, Katsevich A, Lauritsch G and Hornegger J 2005 Exact and efficient cone-beam reconstruction algorithm for a short-scan circle combined with various lines *Proc. SPIE* **5747** 388–99
- Fahrig R and Holdsworth D 2000 Three-dimensional computed tomographic reconstruction using a c-arm mounted: xrii. Image-based correction of gantry motion nonidealities *Med. Phys.* **27** 30–8
- Faugeras O 1996 *Three-Dimensional Computer Vision: A Geometric Viewpoint* 2nd edn (Cambridge, MA: MIT Press)
- Hartley R and Zisserman A 2003 *Multiple View Geometry in Computer Vision* 2nd edn (Cambridge: Cambridge University Press)

- Hoppe S, Dennerlein F, Lauritsch G, Hornegger J and Noo F 2006 Cone-beam tomography from short-scan circle-plus-arc data measured on a c-arm system *2006 IEEE Nuclear Science Symposium Conference Record* vol 6, pp 2873–7
- Katsevich A 2005 Image reconstruction for the circle-and-arc trajectory *Phys. Med. Biol.* **50** 2249–65
- Noo F, Clackdoyle R, Mennessier C, White T and Roney T 2000 Analytic method based on identification of ellipse parameters for scanner calibration in cone-beam tomography *Phys. Med. Biol.* **45** 3489–508
- Pack J and Noo F 2005 Cone-beam reconstruction using 1D filtering along the projection of *m*-lines *Inverse Problems* **21** 1105–20
- Strobel N, Heigl B, Brunner T, Schütz O, Mitschke M, Wiesent K and Mertelmeier T 2003 Improving 3D image quality of x-ray c-arm imaging systems by using properly designed pose determination systems for calibrating the projection geometry *Proc. SPIE* **5030** 943–54
- Strubel G, Clackdoyle R, Mennessier C and Noo F 2005 Analytic calibration of cone-beam scanners *2005 IEEE Nuclear Science Symposium Conference Record* vol 5, pp 2731–5
- Turbell H 2001 Cone-beam reconstruction using filtered backprojection *PhD Thesis* University of Linköping, Department of Electrical Engineering, SE-581 83 Linköping, Sweden
- Smekal L, Kachelrieß M, Stepina E and Kalender W 2004 Geometric misalignment and calibration in cone-beam tomography *Med. Phys.* **31** 3242–66
- Wiesent K, Barth K, Navab N, Durlak P, Brunner T, Schuetz O and Seissler W 2000 Enhanced 3D-reconstruction algorithm for c-arm systems suitable for interventional procedures *IEEE Trans. Med. Imaging* **19** 391–403
- Yang K, Kwan A, Miller D and Boone J 2006 A geometric calibration method for cone beam CT systems *Med. Phys.* **33** 1695–706